IIETA International Information and Engineering Technology Association
Advancing the World of Information and Engineering

Mathematical Modelling of Engineering Problems
Vol. 13, No. 8, August, 2026, pp. 1025-1035
Journal homepage: http://iieta.org/journals/mmep

Comparative Thermal–Hydraulic and Second-Law Assessment of CuO, Al_2O_3 and TiO_2 Water-Based Nanofluids in a Double-Pipe Heat Exchanger Using a Koo–Kleinstreuer Conductivity Model

Noor Al-Huda A. Taher[1], Zainab H. Kadhim[1*], Fatima Adil Raheemah[2], Lina H. Ali[1]

[1] Department of Mechanical Engineering, College of Engineering, Wasit University, Kut 52001, Iraq
[2] Department of Mechanical Engineering, Faculty of Engineering, University of Misan, Amarah 62001, Iraq

Corresponding Author Email: zainabh@uowasit.edu.iq

Copyright: ©2026 The authors. This article is published by IIETA and is licensed under the CC BY 4.0 license (http://creativecommons.org/licenses/by/4.0/).

https://doi.org/10.18280/mmep.130805

Received: 1 September 2026
Revised: 16 October 2026
Accepted: 24 October 2026
Available online: 31 October 2026

Keywords:
double-pipe heat exchanger, entropy generation, Koo–Kleinstreuer model, MATLAB modelling, nanofluid, thermal–hydraulic performance

ABSTRACT

The particle material of a water-based nanofluid sets the balance between the gain in convective heat transfer and the hydraulic penalty, but the two effects are seldom reported on a common basis. This study compares CuO, Al_2O_3 and TiO_2 water-based nanofluids in a double-pipe heat exchanger under identical geometric and flow conditions. Effective properties were obtained from mixture rules, the Brinkman viscosity relation and a Brownian-corrected Koo–Kleinstreuer conductivity model. Heat transfer was evaluated with the Gnielinski correlation and the effectiveness–NTU method. Irreversibility was quantified with an entropy-generation balance. The MATLAB model was verified against an independent Python implementation and compared with published data. Volume fractions of 0–5%, particle diameters of 30–60 nm and Reynolds numbers of 5,000–50,000 were examined. At a volume fraction of 5% and Re = 20,000, Al_2O_3 gave the largest convective-coefficient enhancement (+13.31%) and the largest pressure-drop increase (+12.37%). CuO gave the smallest pressure-drop increase (+1.88%) and the highest effectiveness (38.65%), and it was the only nanofluid that reduced total entropy generation. CuO also ranked first on the coefficient-based performance criterion (1.1316), followed by Al_2O_3 (1.0941) and TiO_2 (1.0824). For the geometry and conditions examined, the hydraulic penalty therefore discriminates between the materials more strongly than the thermal gain.

1. INTRODUCTION

Heat exchangers are central to energy conversion and recovery in the process, power and food industries, and improving their performance remains one of the most direct routes to lower energy consumption [1, 2]. Two complementary strategies have been pursued: modifying the geometry of the flow passage and replacing the conventional working fluid with a nanofluid. A nanofluid is a colloidal suspension of solid particles of 1–100 nm in a base liquid such as water [2, 3].

Dispersed metal, metal-oxide or carbon-based particles alter the thermophysical properties of the base fluid. The thermal conductivity changes most strongly, but the specific heat and viscosity change as well, so any gain in heat transfer is accompanied by a change in hydraulic behaviour [3]. These property changes have motivated the use of nanofluids in heat exchangers for energy-conversion systems [4], and recent property measurements have extended the range of candidate fluids to multi-component (hybrid) suspensions [5]. Studies [4, 5] presented general background only; neither addressed a straight double-pipe exchanger or a single-material comparison of the type considered in this study.

Most studies of nanofluid exchangers combine a fluid-side modification with a geometric one. Ghazanfari et al. [6] showed by computational fluid dynamics (CFD) that both twisted tubes and Al_2O_3, Cu, CuO or TiO_2 nanofluids (0.05–0.15%) improved the thermal performance of a shell-and-tube exchanger. In double-pipe exchangers, Jasim et al. [7] combined a steel-ball porous medium with an Al_2O_3/water nanofluid. The overall heat-transfer coefficient, the number of transfer units (NTU) and the effectiveness all increased with flow rate and concentration. Jassim and Ahmed [8] measured Nusselt-number gains of up to 23% for Cu/water and 13% for Al_2O_3/water at 0.26–0.83% and Re = 7,000–15,000. They also observed a heat leakage that grew with concentration. Kannadhasan et al. [9] observed a marked increase in heat-transfer rate when a 0.3 wt.% CuO/water nanofluid was used as the cold stream of a counter-flow exchanger.

Fins, inserts and alternative geometries have also been studied. A curved rectangular fin raised the convective coefficient of Al_2O_3 and TiO_2 nanofluids by up to 85% with a lower pressure drop than a straight fin [10]. A helical-coil double-pipe exchanger gave coefficient and Nusselt-number ratios of 1.43 and 1.38 for 1.0 vol.% Al_2O_3/water [11]. Twisted tapes in a porous duct with a hybrid MWCNT–Al_2O_3/water nanofluid improved the Nusselt number by up to 35.6% [12]. In addition, a triangular tube under a non-uniform magnetic field raised the Nusselt number of an Fe_3O_4/water ferrofluid by about 15% [13].

Direct comparisons of particle materials are less common. Salim et al. [14] compared TiO_2, Al_2O_3 and Fe_3O_4 water-based nanofluids (1–10%) in an N-shape double-pipe exchanger. Al_2O_3 gave the highest effectiveness, and the Nusselt number increased by more than 55% at 6%. Ajeeb et al. [15] tested Al_2O_3 nanofluids (0.01–0.20%) in a compact plate exchanger and reported a 27.8% gain in heat-transfer rate at the cost of an 8% increase in pressure drop.

Recent work has refined both the modelling and the material set. Alhulaifi [16] reported a 3.5% gain in the convective coefficient of TiO_2/water (0.2–0.6 vol.%) in a counter-flow double-pipe exchanger at Re = 4,000–18,000. Other studies examined Fe_3O_4/water against condensing R-134a vapour (up to 13.4%) [17] and CuO nanofluids with baffles and turbulators (Nusselt-number gains of up to about 350%) [18]. Gains of 35% and of up to 48.8% were reported for an MgO–carboxymethyl-cellulose suspension in a U-bend exchanger [19] and for Al_2O_3 and CuO nanofluids in annular curved tubes [20], respectively. An $MnCoFeO_4$/water nanofluid optimised by response-surface methodology gave a 40% gain with a 15.4% rise in friction [21], and Al_2O_3, CuO and hexagonal boron-nitride nanofluids at 5–10% were analysed with CFD and an artificial neural network [22].

The studies reviewed above differ in their relevance to the present configuration. Studies [6, 7, 10-13, 17-21] involved at least one feature absent from the present configuration: another exchanger type, a curved, helical or U-bend passage, inserts, porous media, a magnetic field, cold-side phase change or a hybrid suspension. They illustrate the range of available enhancement mechanisms, but their results are not directly comparable with those of a smooth, straight double-pipe exchanger. Studies [8, 9, 16] examined straight double-pipe exchangers with single-material water-based nanofluids and are therefore the closest counterparts of the present work. Studies [14, 15, 22], in contrast, compared several particle materials in other geometries or at other concentrations.

Three gaps follow from this review. First, most studies cover a narrow concentration range, so the sensitivity of the response to volume fraction is not resolved systematically. Second, the thermal gain and the hydraulic penalty are usually reported separately, although it is their balance that determines whether a nanofluid is beneficial. Combined thermal–hydraulic and second-law assessments on a common basis remain rare. Third, the predicted enhancement depends strongly on the conductivity model, yet the model is seldom stated, which hinders comparison between studies.

The present study addresses these gaps for a smooth, straight double-pipe exchanger. CuO, Al_2O_3 and TiO_2 water-based nanofluids are compared in a single configuration over wide ranges of volume fraction, particle diameter and Reynolds number, using the Brownian-corrected Koo–Kleinstreuer conductivity model. The convective-coefficient enhancement, the pressure-drop penalty, two performance criteria and the entropy generation are reported on a common basis. The study makes two contributions. First, a like-for-like ranking on thermal, hydraulic, energy-efficiency and second-law criteria shows that, for the geometry and operating conditions considered, the material with the largest thermal enhancement is not the best overall choice. Second, a compact closed-form correlation for the convective-coefficient ratio is proposed for design estimates within its stated validity range.

2. PHYSICAL MODEL

2.1 Geometry and operating conditions

The exchanger consists of two concentric copper tubes (Figure 1). The nanofluid flows in the inner tube as the hot stream, and cooling water flows in the annulus as the cold stream. Both counter-flow and parallel-flow arrangements were considered. The geometric parameters are listed in Table 1. The dimensions lie at the lower end of the standard range for double-pipe hairpins [23]. In this range, the outer pipe has an inner diameter of 50–400 mm, the inner tube an outer diameter of 19–100 mm and each section a nominal length of 1.5–12 m. The resulting length-to-diameter ratio of 182 is close to the ratios of 131–200 used in the experiments of Aghayari et al. [24]. The operating conditions and the parameter ranges are summarised in Table 2.

The hot-side inlet temperature (50–90 °C) is distinct from the temperature at which the properties were evaluated. The evaluation temperature is the bulk-mean value $T_{avg} = (T_{h,in} + T_{c,in})/2$. It equals 45 °C (318.15 K) in the reference case and ranges from 35 to 55 °C (308.15–328.15 K) over the inlet-temperature sweep. This range lies inside the 298–363 K validity interval of the adopted conductivity model [25, 26]. The hot-side inlet temperatures themselves (323.15–363.15 K) also fall inside this interval. The non-zero volume fractions (1–5%) lie within the 1–10% interval over which the Brownian coefficients were fitted by Vajjha and Das [26].

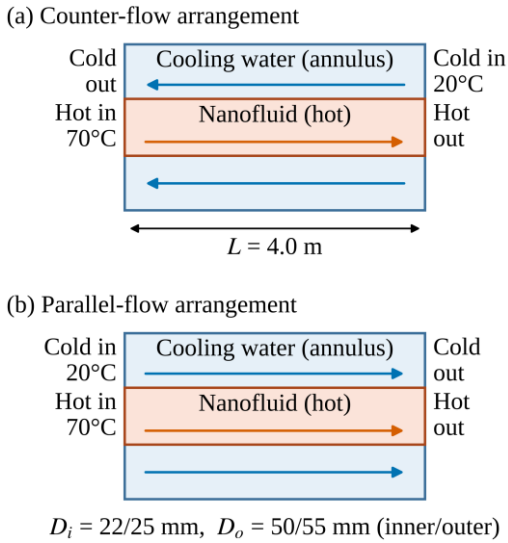


Figure 1. Schematic of the double-pipe heat exchanger: (a) counter-flow arrangement; (b) parallel-flow arrangement

Table 1. Geometric parameters of the double-pipe heat exchanger

Parameter	Symbol	Value
Inner tube, inner diameter	$D_{i,in}$	22 mm
Inner tube, outer diameter	$D_{i,out}$	25 mm
Outer tube, inner diameter	$D_{o,in}$	50 mm
Outer tube, outer diameter	$D_{o,out}$	55 mm
Exchanger length	L	4.0 m
Annulus hydraulic diameter	D_h	25 mm
Inner heat-transfer area	A_i	0.2765 m²
Outer heat-transfer area	A_o	0.3142 m²
Length-to-diameter ratio	$L/D_{i,in}$	182
Wall material / conductivity	k_{wall}	Copper, 385 W m⁻¹ K⁻¹

Table 2. Operating conditions and study parameters

Parameter	Symbol	Value / Range
Hot-side inlet temperature	$T_{h,in}$	70 °C (50–90 °C studied)
Cold-side inlet temperature	$T_{c,in}$	20 °C
Bulk-mean (evaluation) temperature	T_{avg}	45 °C (35–55 °C)
Cold-side mass flow rate	$\dot{m}_c$	0.25 kg s^{-1}
Reynolds number (inner tube)	Re	5,000; 10,000; 20,000; 35,000; 50,000
Volume fraction	φ	0, 1, 2, 3, 4, 5%
Particle diameter	d_p	30, 45, 60 nm
Particle material	–	Al_2O_3, CuO, TiO_2
Flow arrangement	–	Parallel, counter
Total number of cases	–	460 (450 nanofluid + 10 base fluid)

Note: $T_{avg} = (T_{h,in} + T_{c,in})/2$; the value in brackets is its range over the inlet-temperature sweep. The case count is derived in Section 4.

The base-fluid properties in Table 3 correspond to water at 40 °C. They were held constant at these values in all calculations and were not interpolated to T_{avg}. The evaluation temperature therefore enters the model only through the Brownian term of Eq. (6), that is, through the factor $(k_B T)^{1/2}$ and the function $g(T, \varphi)$ of Eq. (8). This convention was applied uniformly to all tables, figures and captions. A check with water properties at 45 °C changed the relative enhancements of the convective coefficient and of the pressure drop at φ = 5% by less than 0.3 percentage points and did not change the ranking of the three materials.

Table 3. Properties of the base fluid and the nanoparticles

Material	ρ (kg m^{-3})	c_p (J kg^{-1} K^{-1})	k (W m^{-1} K^{-1})	d_p (nm)
Water (40 °C)	992.0	4178	0.631	–
Al_2O_3	3970	765	40.0	30 / 45 / 60
CuO	6320	540	76.5	30 / 45 / 60
TiO_2	4250	686	8.4	30 / 45 / 60

Note: The viscosity of water at 40 °C, 0.653 mPa s, was used in Eq. (3). The water properties were held at these values in all calculations (Section 2.1).

2.2 Assumptions

The analysis was based on the assumptions that are standard for single-phase treatments of nanofluid exchangers [14, 27, 28]. The flow in both streams was taken as steady, incompressible, turbulent and fully developed. The suspension was treated as a uniformly dispersed, single-phase Newtonian fluid with no slip between the particles and the base fluid. The properties were held constant, with the base-fluid properties taken from Table 3 [25, 26, 29] and the Brownian term evaluated at T_{avg}. Axial conduction and heat loss to the surroundings were neglected. The inner-tube flow was specified by its Reynolds number, and the annulus flow by its mass flow rate.

3. MATHEMATICAL FORMULATION

3.1 Nanofluid properties

The density and the specific heat follow the mixture rule of Pak and Cho [29] and the thermal-equilibrium formulation of Xuan and Roetzel [30], respectively. In the latter, the constituents are weighted by mass rather than by volume:

$$\rho_{nf} = (1-\varphi)\rho_{bf} + \varphi\rho_p \tag{1}$$

$$c_{p,nf} = \frac{(1-\varphi)(\rho c_p)_{bf} + \varphi(\rho c_p)_p}{\rho_{nf}} \tag{2}$$

The viscosity is obtained from the Brinkman relation [31], which remains the most widely used expression for dilute suspensions:

$$\mu_{nf} = \frac{\mu_{bf}}{(1-\varphi)^{2.5}} \tag{3}$$

Eq. (3) depends only on the volume fraction. All three nanofluids therefore have the same viscosity at a given φ. This equality is a consequence of the adopted model and not an independent material result.

The effective thermal conductivity requires closer attention, because the choice of model has a first-order effect on the predicted enhancement. The classical model of Maxwell [32], later extended to non-spherical particles by Hamilton and Crosser [33], depends only on the volume fraction and the conductivity ratio. It contains neither a length scale nor the temperature and therefore cannot represent the Brownian contribution. Koo and Kleinstreuer [25] resolved this limitation by splitting the conductivity into a static part and a Brownian part:

$$k_{nf} = k_{static} + k_{Brownian} \tag{4}$$

$$k_{static} = k_{bf}\frac{k_p + 2k_{bf} - 2\varphi(k_{bf} - k_p)}{k_p + 2k_{bf} + \varphi(k_{bf} - k_p)} \tag{5}$$

$$k_{Brownian} = 5\times10^4\,\beta\,\varphi\,\rho_{bf}\,c_{p,bf}\sqrt{\frac{k_B T}{\rho_p d_p}}\;g(T,\varphi) \tag{6}$$

Eq. (5) is the Maxwell result, and Eq. (6) is the Brownian term, with T in K and d_p in m. The coefficient β and the function $g(T, \varphi)$ were taken from the correlations of Vajjha and Das [26]. The function is written here as g to avoid confusion with the friction factor f. The implemented expressions, with φ as a fraction, are:

$$\beta_{Al_2O_3} = 8.4407\,(100\varphi)^{-1.07304}$$
$$\beta_{CuO} = 9.8810\,(100\varphi)^{-0.9446} \tag{7}$$

$$g(T,\varphi) = (2.8217\times10^{-2}\varphi + 3.917\times10^{-3})\frac{T}{T_0} - (3.0669\times10^{-2}\varphi + 3.91123\times10^{-3}) \tag{8}$$

where T_0 = 273 K. Vajjha and Das [26] did not report a coefficient for TiO_2–water. The Al_2O_3 expression for β was therefore used for TiO_2 as an approximation. This substitution affects only the Brownian part of the TiO_2 conductivity. Consequently, all TiO_2 results that depend on k_{nf} depend on the substitution, whereas the TiO_2 density, specific heat and viscosity do not. At φ = 3%, d_p = 30 nm and 45 °C, the Brownian part accounts for 0.0682 W m^{-1} K^{-1} of the TiO_2 conductivity of 0.7460 W m^{-1} K^{-1} (9.1%). Because d_p appears in the denominator under the square root of Eq. (6), the model predicts a stronger enhancement for finer particles, a trend also reported numerically by Saha and Paul [28].

3.2 Heat transfer and pressure drop

The Reynolds and Prandtl numbers of the inner-tube flow are formed from the nanofluid properties:

$$Re = \frac{4\dot{m}_\mathrm{h}}{\pi D_\mathrm{i,in}\mu_\mathrm{nf}}, \qquad Pr = \frac{\mu_\mathrm{nf} c_\mathrm{p,nf}}{k_\mathrm{nf}} \tag{9}$$

The Nusselt number was obtained from the Gnielinski correlation [34] rather than the older Dittus–Boelter form [35]. The Gnielinski correlation covers the whole Reynolds-number range considered here and agrees well with single-phase simulations of this geometry [27]. The Darcy friction factor was obtained from the Petukhov relation [36]:

$$Nu = \frac{(f/8)(Re - 1000)\,Pr}{1 + 12.7\sqrt{f/8}\,(Pr^{2/3} - 1)} \tag{10}$$

$$f = (0.790 \ln Re - 1.64)^{-2} \tag{11}$$

The pressure drop and the pumping power of the inner-tube stream follow from the Darcy–Weisbach relation. Because the comparison was made at a fixed Reynolds number, the mass flow rate and the mean velocity follow from Eq. (9) as $\dot{m}_\mathrm{h} = \pi D_\mathrm{i,in}\mu_\mathrm{nf} Re/4$ and $v = Re\,\mu_\mathrm{nf}/(\rho_\mathrm{nf} D_\mathrm{i,in})$, which gives:

$$\Delta P = f\frac{L}{D_\mathrm{i,in}}\frac{\rho_\mathrm{nf} v^2}{2} = \frac{f(Re)\,L\,Re^2\mu_\mathrm{nf}^2}{2\rho_\mathrm{nf} D_\mathrm{i,in}^3}, \qquad P = \frac{\dot{m}_\mathrm{h}\,\Delta P}{\rho_\mathrm{nf}} \tag{12}$$

At a fixed *Re*, the friction factor is the same for all fluids, and the pressure drop therefore scales with $\mu_\mathrm{nf}^2/\rho_\mathrm{nf}$. The fixed-*Re* basis was adopted because it preserves dynamic similarity between the fluids and is commonly used in single-phase studies of turbulent nanofluid flow in tubes (e.g., studies [28, 37]). A comparison at a fixed mass flow rate or velocity would weight viscosity and density differently and could change the hydraulic ranking.

The overall heat-transfer coefficient, based on the inner area A_i, combines the three thermal resistances in series, and the duty follows from the effectiveness–NTU method:

$$\frac{1}{UA_\mathrm{i}} = \frac{1}{h_\mathrm{i}A_\mathrm{i}} + \frac{\ln\left(D_\mathrm{i,out}/D_\mathrm{i,in}\right)}{2\pi k_\mathrm{wall} L} + \frac{1}{h_\mathrm{o}A_\mathrm{o}} \tag{13}$$

$$NTU = \frac{UA_\mathrm{i}}{C_\mathrm{min}}, \quad C_\mathrm{r} = \frac{C_\mathrm{min}}{C_\mathrm{max}}, \quad Q = \varepsilon\, C_\mathrm{min}\left(T_\mathrm{h,in} - T_\mathrm{c,in}\right) \tag{14}$$

where $C = \dot{m}c_\mathrm{p}$ is the heat-capacity rate. The effectiveness of the counter-flow and parallel-flow arrangements is:

$$\varepsilon_\mathrm{cf} = \frac{1 - \exp[-NTU(1 - C_\mathrm{r})]}{1 - C_\mathrm{r}\exp[-NTU(1 - C_\mathrm{r})]} \tag{15}$$

$$\varepsilon_\mathrm{pf} = \frac{1 - \exp[-NTU(1 + C_\mathrm{r})]}{1 + C_\mathrm{r}} \tag{16}$$

The axial temperature profiles follow from the local energy balances of the two streams with the constant *U* of Eq. (13):

$$\frac{dT_\mathrm{h}}{dx} = -\frac{U\pi D_\mathrm{i,in}}{C_\mathrm{h}}\left(T_\mathrm{h} - T_\mathrm{c}\right), \qquad \frac{dT_\mathrm{c}}{dx} = \pm\frac{U\pi D_\mathrm{i,in}}{C_\mathrm{c}}\left(T_\mathrm{h} - T_\mathrm{c}\right) \tag{17}$$

The upper sign applies to parallel flow and the lower sign to counter flow. Because *U* and the properties are constant, Eq. (17) has the closed-form solution $(T_\mathrm{h} - T_\mathrm{c})(x) = (T_\mathrm{h} - T_\mathrm{c})(0)\exp[-U\pi D_\mathrm{i,in}x(1/C_\mathrm{h} \pm 1/C_\mathrm{c})]$. The profiles therefore contain no information beyond the ε–NTU solution, and their outlet temperatures coincide with those of Eqs. (14)–(16). No property updating along the exchanger was performed.

3.3 Performance criteria and irreversibility

Two performance-evaluation criteria (PEC) were used. The first is the Nusselt-based form common in the nanofluid literature [37, 38]. The second replaces the Nusselt number by the convective coefficient and the friction factor by the pumping power of Eq. (12):

$$PEC = \frac{Nu/Nu_0}{(f/f_0)^{1/3}}, \qquad PEC_\mathrm{h} = \frac{h_\mathrm{i}/h_\mathrm{i,0}}{(P/P_0)^{1/3}} \tag{18}$$

The subscript 0 denotes the base fluid at the same *Re*, arrangement and inlet temperatures. The reference pumping power P_0 was calculated from Eq. (12) with the water properties of Table 3. Because *Re* is fixed, the mass flow rate differs between each nanofluid and the base fluid ($\dot{m}_\mathrm{h} \propto \mu_\mathrm{nf}$), and this difference is included in P/P_0. An energy-efficiency ratio was also evaluated:

$$EER = \frac{Q/Q_0}{P/P_0} \tag{19}$$

The irreversibility was quantified with an entropy balance over the whole exchanger, following Bejan [39]. The total entropy-generation rate is the sum of a thermal and a frictional contribution:

$$\dot{S}_\mathrm{gen} = \dot{S}_\mathrm{gen,th} + \dot{S}_\mathrm{gen,fr}, \qquad \dot{S}_\mathrm{gen,th} = C_\mathrm{h}\ln\frac{T_\mathrm{h,out}}{T_\mathrm{h,in}} + C_\mathrm{c}\ln\frac{T_\mathrm{c,out}}{T_\mathrm{c,in}} \tag{20}$$

$$\dot{S}_\mathrm{gen,fr} = \frac{\dot{m}_\mathrm{h}\Delta P_\mathrm{h}}{\rho_\mathrm{nf}\bar{T}_\mathrm{h}} + \frac{\dot{m}_\mathrm{c}\Delta P_\mathrm{c}}{\rho_\mathrm{bf}\bar{T}_\mathrm{c}} \tag{21}$$

All temperatures in Eqs. (20) and (21) are absolute temperatures in K. The hot-side term of Eq. (20) is negative and the cold-side term is positive; their sum is positive. The frictional term includes both streams, with ΔP_c calculated for the annulus with the same friction relation. The mean temperatures are $\bar{T}_\mathrm{h} = (T_\mathrm{h,in} + T_\mathrm{h,out})/2$ and $\bar{T}_\mathrm{c} = (T_\mathrm{c,in} + T_\mathrm{c,out})/2$. Replacing them by logarithmic-mean temperatures changed none of the reported entropy measures in the fourth decimal place. The Bejan number *Be* and the augmentation entropy-generation number $N_\mathrm{s,a}$ are defined as:

$$Be = \frac{\dot{S}_\mathrm{gen,th}}{\dot{S}_\mathrm{gen}}, \qquad N_\mathrm{s,a} = \frac{\dot{S}_\mathrm{gen}}{\dot{S}_\mathrm{gen,0}} \tag{22}$$

A value of $N_\mathrm{s,a}$ below unity indicates that the nanofluid reduces the total entropy generation relative to the base fluid under the same conditions.

4. MATLAB IMPLEMENTATION

The model was implemented in MATLAB. Because the

properties are constant and the effectiveness–NTU relations return the duty in closed form, no partial-differential solver is required, and each operating point is obtained in a single forward pass. This makes the code faster to develop and easier to audit than a general-purpose CFD model. The code comprises three parts: a property routine implementing Eqs. (1)–(8); a single-point solver returning Re, Pr, the two convective coefficients, U, NTU, ε, Q, the outlet temperatures, ΔP, P and the entropy terms of Eqs. (20)–(22); and a driver that sweeps the parameter space. No toolbox is required.

The parametric study comprised 460 operating points. The six volume fractions in Table 2 include $\varphi = 0$, at which the fluid is pure water irrespective of the particle material and diameter. The nanofluid cases therefore comprise three materials × five non-zero volume fractions × three particle diameters × five Reynolds numbers × two arrangements = 450 points. The base fluid was evaluated once for each Reynolds number and arrangement (5 × 2 = 10 points), giving 450 + 10 = 460 points in total. A further 1,575 points were generated for the correlation of Section 6.5. The complete sweep runs in a few seconds on a standard desktop computer. Two coding errors were identified and corrected during code review: the reserved keyword *if* had been used as a loop index, and the structure fields were ordered inconsistently between two branches of the property routine. Neither error affected the results reported here.

5. VERIFICATION

5.1 Independent cross-check of the MATLAB code

Before any result was interpreted, the whole procedure was transcribed independently into Python 3, and the two implementations were compared variable by variable. The test matrix comprised three materials, four volume fractions (0, 1, 3 and 5%), three particle diameters (30, 45 and 60 nm) and three Reynolds numbers (5,000, 20,000 and 50,000). It also included two flow arrangements, two conductivity models (Maxwell and Koo–Kleinstreuer) and three hot-side inlet temperatures (50, 70 and 90 °C). This gives 3 × 4 × 3 × 3 × 2 × 2 × 3 = 1,296 operating points. At each point, 21 output quantities were compared: ρ_{nf}, $c_{p,nf}$, μ_{nf}, k_{nf}, Pr, Nu, f, h_i, U, NTU, ε, Q, ΔP, P, $\dot{m}_h$, $T_{h,out}$, $T_{c,out}$, $\dot{S}_{gen,th}$, $\dot{S}_{gen,fr}$, $\dot{S}_{gen}$ and Be. In total, 27,216 comparisons were made. The largest relative deviation was 4.24×10^{-14}%, at the level of double-precision round-off. This result confirms that the MATLAB code is free of transcription errors. It does not, by itself, validate the physical model.

5.2 Comparison with published data

To place the predictions in the context of published results, the model was compared with four published studies (Table 4). The comparison was made for Al_2O_3–water at φ = 3%, the only condition available in all four studies. The present value, Δh = 10.30%, corresponds to d_p = 30 nm, Re = 20,000 and counter flow. The deviation is defined as $|\Delta h_{present} - \Delta h_{ref}|/\Delta h_{ref} \times 100$. The reference studies differ from the present one in geometry, Reynolds number, particle size or method, as listed in Table 4. The comparison is therefore presented as a consistency check and as qualitative context, not as a quantitative validation.

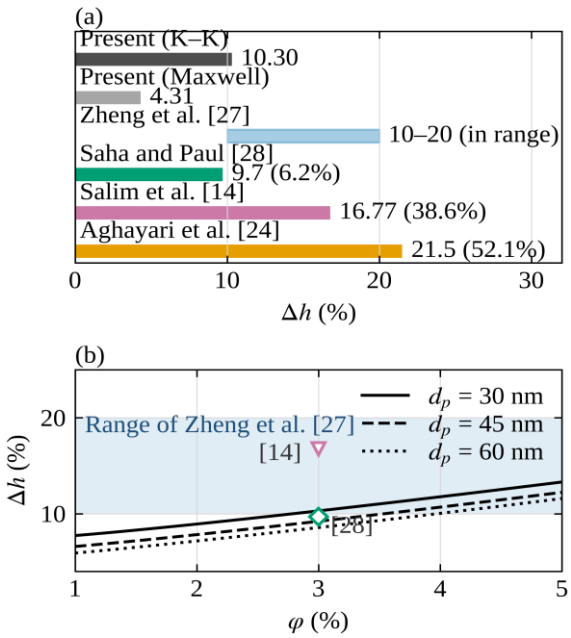


Figure 2. Comparison with previous studies for Al_2O_3–water at Re = 20,000: (a) convective-coefficient enhancement reported by each study, with the deviation from the present model in brackets; (b) present model for three particle diameters against the range of Zheng et al. [27] and the values of studies [14, 28] at φ = 3%

Table 4. Comparison of the convective-coefficient enhancement Δh for Al_2O_3–water (φ = 3%) with published studies

Study	Configuration and Method	Reference Δh (%)	Deviation (%)	Role in the Comparison
Present (Koo–Kleinstreuer)	Straight double-pipe, single-phase, Gnielinski; d_p = 30 nm, Re = 20,000	+10.30	–	–
Present (Maxwell)	As above, Maxwell conductivity	+4.31	–	–
Zheng et al. [27]	Straight double-pipe inner tube, single-phase, Gnielinski	10–20 (range)	Inside range	Consistency check (same method)
Saha and Paul [28]	Straight circular pipe, single-phase, turbulent	≈9.7	6.2	Consistency check (same method)
Salim et al. [14]	N-shape double-pipe (secondary flows)	+16.77	38.6	Qualitative context
Aghayari et al. [24]	Experimental double-pipe, lower φ	+21.5	52.1	Qualitative context

Note: Deviation = $|\Delta h_{present} - \Delta h_{ref}|/\Delta h_{ref} \times 100$, with $\Delta h_{present}$ = 10.30%. Reference values were taken at φ = 3% where reported; the Reynolds numbers and particle sizes of the reference studies differ from those of the present case.

The study of Zheng et al. [27] is closest to the present one in method: a straight double-pipe exchanger, a single-phase treatment of the nanofluid and the same Gnielinski correlation. The present prediction of 10.30% at 3% lies inside the 10–20% range that they report, and the agreement holds at 4% and 5%. Against Saha and Paul [28], who used a circular pipe and the same single-phase approach, the deviation is 6.2%. The two remaining comparisons deviate considerably more, for

structural rather than numerical reasons. Salim et al. [14] studied an N-shaped exchanger, whose bends generate secondary flows that are absent in a straight pipe, so a higher enhancement is expected. Aghayari et al. [24] reported experimental measurements, which single-phase models are known to under-predict because they do not resolve particle migration or thermophoretic drift [28]. These two studies are therefore treated as context rather than as validation (Figure 2).

6. RESULTS AND DISCUSSION

6.1 Effective properties and the conductivity model

Table 5 lists the properties at φ = 3%. Adding particles increased the density, thermal conductivity and viscosity and decreased the specific heat. The net effect was a reduction of about 18% in the Prandtl number, because the increase in conductivity outweighed the increase in viscosity. CuO had the highest density and the lowest specific heat of the three nanofluids, whereas Al_2O_3 had the lowest density and the highest specific heat. The effective conductivity was highest for CuO (0.7635 W m^{-1} K^{-1}) and lowest for TiO_2 (0.7460 W m^{-1} K^{-1}), in line with the particle conductivities in Table 3. Figure 3 shows the four properties over the whole concentration range.

The choice of conductivity model matters as much as the effect under study. At φ = 3%, the Maxwell expression [32] gives a conductivity enhancement of 8.8%, whereas the Koo–Kleinstreuer model [25] gives 20.0%, a factor of 2.3. The difference carries through to the convective coefficient, for which the two models predict 4.3% and 10.3%, respectively (Figure 4). An enhancement reported without its conductivity model is therefore difficult to interpret, and the model is stated explicitly throughout this work.

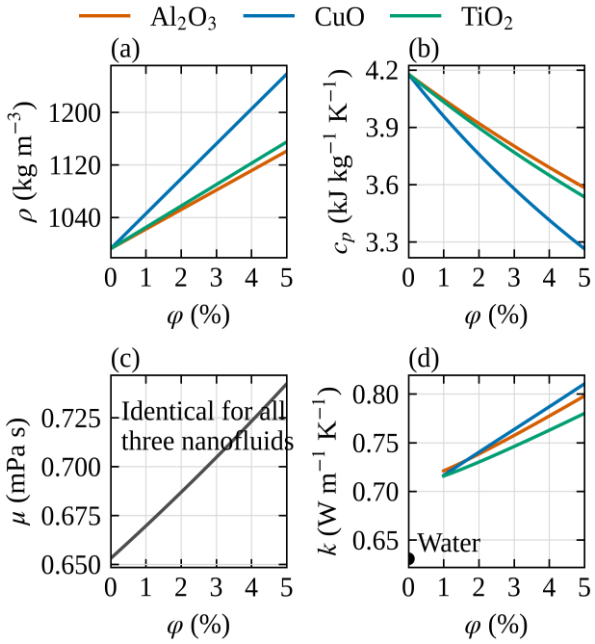


Figure 3. Thermophysical properties of the nanofluids: (a) density; (b) specific heat; (c) viscosity; (d) thermal conductivity (shown over φ = 1–5%, the fitted range of the Brownian coefficients)

Table 5. Nanofluid properties at φ = 3% and d_p = 30 nm

Fluid	ρ (kg m^{-3})	c_p (J kg^{-1} K^{-1})	μ (mPa s)	k (W m^{-1} K^{-1})	Pr
Water	992.0	4178.0	0.6530	0.6310	4.324
Al_2O_3–water	1081.3	3802.1	0.7047	0.7574	3.537
CuO–water	1151.8	3579.2	0.7047	0.7635	3.303
TiO_2–water	1089.7	3769.4	0.7047	0.7460	3.560

Note: The Brownian term was evaluated at T_{avg} = 45 °C, and the base-fluid properties were taken from Table 3. The properties were calculated from Eqs. (1)–(8); the equal viscosities follow from the Brinkman relation, Eq. (3).

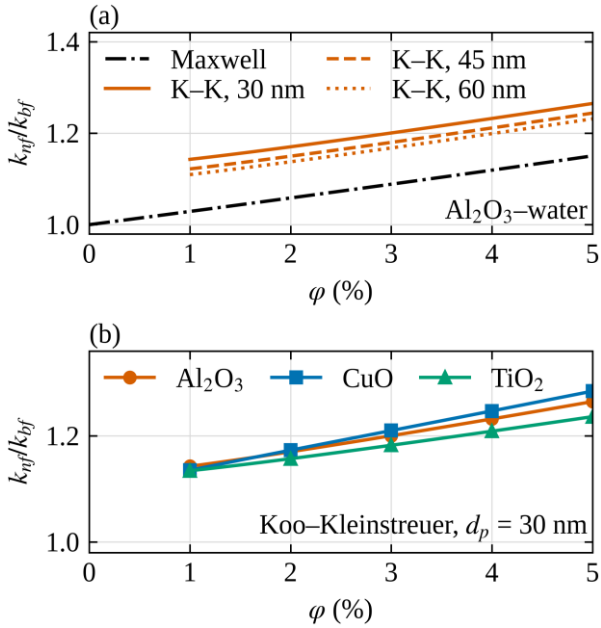


Figure 4. Thermal-conductivity ratio: (a) Maxwell [32] and Koo–Kleinstreuer (K–K) [25] models for Al_2O_3–water at three particle diameters; (b) material comparison (K–K, d_p = 30 nm)

6.2 Thermal–hydraulic performance

Table 6 lists the performance at Re = 20,000 in counter flow. All three nanofluids increased the convective coefficient monotonically with concentration. Al_2O_3 gave the largest convective-coefficient enhancement, from 7.72% at 1% to 13.31% at 5%, followed by TiO_2. CuO gave the smallest enhancement despite having the most conductive particles. The specific heat explains this result: CuO has the lowest specific heat, so its Prandtl number decreases the most, and this reduction partly cancels the gain in conductivity.

Table 6. Performance at Re = 20,000, d_p = 30 nm, counter flow (Eqs. (9)–(16))

Fluid	φ (%)	h_i	Δh (%)	ε (%)	Q (W)	ΔP (Pa)	$\Delta(\Delta P)$ (%)
Water	0	3499.4	–	34.07	16,062	844.6	–
Al_2O_3	1	3769.7	+7.72	35.11	16,433	862.2	+2.09
Al_2O_3	3	3859.8	+10.30	35.69	16,521	902.2	+6.83
Al_2O_3	5	3965.1	+13.31	36.19	16,637	949.0	+12.37
CuO	1	3720.7	+6.32	35.59	16,301	842.8	−0.21
CuO	3	3778.5	+7.97	37.24	16,228	847.0	+0.29
CuO	5	3841.5	+9.77	38.65	16,184	860.4	+1.88
TiO_2	1	3748.9	+7.13	35.13	16,395	859.8	+1.81
TiO_2	3	3812.4	+8.94	35.80	16,432	895.3	+6.01
TiO_2	5	3891.0	+11.19	36.38	16,500	937.5	+11.01

Note: h_i in W m^{-2} K^{-1}. The overall coefficient U is shown in Figure 5(b).

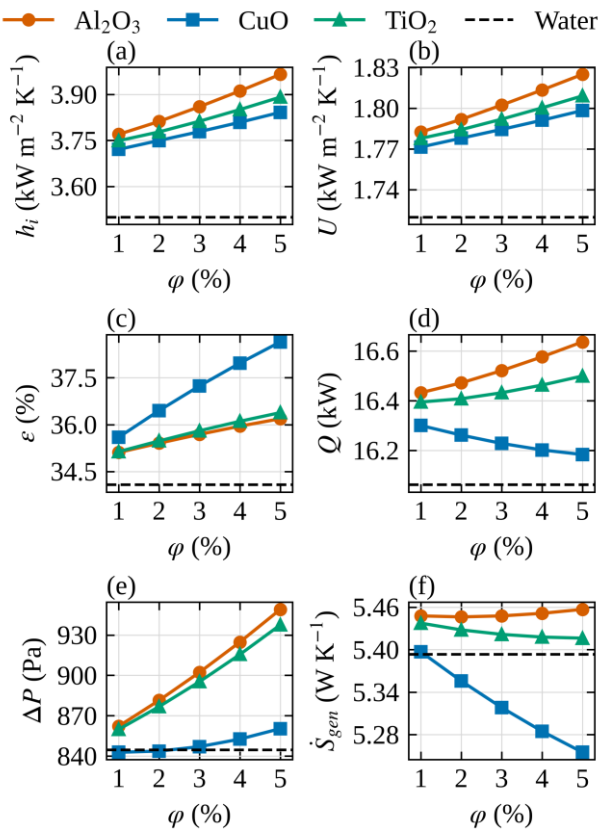


Figure 5. Variation with concentration (Re = 20,000, d_p = 30 nm, counter flow; dashed line: water): (a) h_i; (b) U; (c) effectiveness; (d) heat duty; (e) pressure drop; (f) entropy generation

The ordering reversed for the effectiveness: CuO reached 38.65% at 5%, compared with 36.19% for Al_2O_3. Its low specific heat reduces the minimum heat-capacity rate and thereby increases NTU. The duty followed a different ordering again. Because $Q = \varepsilon C_{min}(T_{h,in} - T_{c,in})$, the smaller C_{min} offset the higher effectiveness, and Al_2O_3 transferred the most heat (16,637 W, compared with 16,184 W for CuO). The preferred material therefore depends on whether the design objective is maximum duty or maximum effectiveness. Figure 5 shows these quantities as functions of concentration.

6.3 Hydraulic penalty and performance criteria

The hydraulic penalty separated the three nanofluids more sharply than the thermal gain did. At φ = 5%, the pressure drop increased by 12.37% for Al_2O_3 and by 11.01% for TiO_2, but by only 1.88% for CuO. The calculation basis explains this difference. At a fixed Re, Eq. (12) gives $\Delta P \propto \mu_{nf}^2/\rho_{nf}$, because the friction factor and the geometry are common to all fluids. At a given φ, the Brinkman relation gives the same viscosity, and hence the same mass flow rate, for the three nanofluids. The differences between materials at equal φ therefore arise from the density alone, and CuO, the densest of the three, has the smallest pressure drop. This density effect is thus a consequence of the fixed-Re basis and of the Brinkman relation, not an independent hydraulic property of the material. The effect on pumping power was even larger: at 1%, CuO required 2.9% less pumping power than pure water.

The two criteria of Eq. (18) led to different conclusions. The Nusselt-based criterion was below unity for all three nanofluids, whereas the coefficient-based criterion exceeded unity for all three. This difference results from the normalisation. Because $Nu = h_i D_{i,in}/k_{nf}$ and, at 3%, the conductivity increased by about 20% while the coefficient increased by about 10%, the Nusselt-number ratio necessarily fell even though h_i increased. For a fixed exchanger geometry, the duty depends on h_i through U, not on Nu. The coefficient-based criterion was therefore used to rank the nanofluids in this study. On this basis, CuO ranked first (PEC_h = 1.1316), followed by Al_2O_3 (1.0941) and TiO_2 (1.0824). This ranking applies to the present geometry, the fixed-Re basis and the operating conditions of Table 2. It should not be generalised to other configurations without further analysis. Figure 6 presents the three criteria.

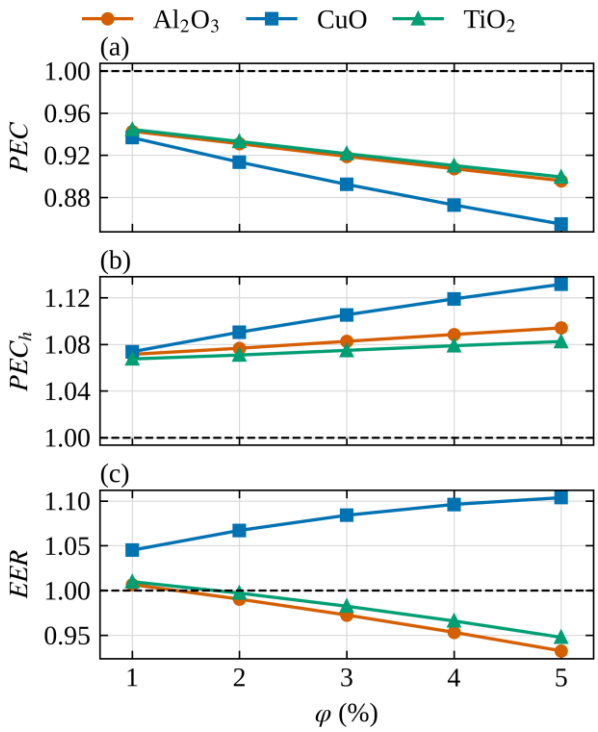


Figure 6. Performance-evaluation criteria (Re = 20,000, d_p = 30 nm, counter flow): (a) Nusselt-based, Eq. (18) [37, 38]; (b) coefficient-based, Eq. (18); (c) energy-efficiency ratio, Eq. (19)

6.4 Particle diameter and inlet temperature

Because the Koo–Kleinstreuer model retains the Brownian term, the particle diameter enters explicitly through the inverse square root in Eq. (6). Reducing the diameter of Al_2O_3 particles from 60 to 30 nm increased the conductivity enhancement from 16.72% to 20.03% and the convective-coefficient enhancement from 8.56% to 10.30% at φ = 3% and Re = 20,000. Saha and Paul [28] reported the same direction of dependence, which the classical mixture models [32, 33] cannot capture because they contain no length scale.

The Brownian term also introduces a strong temperature dependence. When the hot-side inlet temperature was raised from 50 to 90 °C (T_{avg} = 35 – 55 °C), the conductivity enhancement of Al_2O_3–water at 5% increased from 23.4% to 29.7% and the convective-coefficient enhancement from 11.8% to 15.1%. The ordering of the three materials was preserved throughout. A classical mixture model predicts no such dependence, so this behaviour is entirely a consequence of the conductivity model.

6.5 Flow arrangement, entropy generation and correlation

The counter-flow arrangement transferred more heat in every case (Table 7): by 5.09% for pure water and by 5.57–6.02% for the nanofluids, so the margin widened slightly with concentration. The axial profiles in Figure 7, obtained from Eq. (17), explain this result: counter flow maintains a nearly uniform temperature difference along the exchanger, whereas in parallel flow the difference decreases towards the outlet.

Table 7. Effect of flow arrangement at Re = 20,000, d_p = 30 nm (pf: parallel flow; cf: counter flow)

Fluid	φ (%)	ε_{pf} (%)	ε_{cf} (%)	Q_{pf} (W)	Q_{cf} (W)	Gain (%)
Water	0	32.42	34.07	15,284	16,062	+5.09
Al_2O_3	3	33.80	35.69	15,648	16,521	+5.58
Al_2O_3	5	34.23	36.19	15,736	16,637	+5.73
CuO	3	35.21	37.24	15,345	16,228	+5.76
CuO	5	36.46	38.65	15,265	16,184	+6.02
TiO_2	3	33.92	35.80	15,566	16,432	+5.57
TiO_2	5	34.42	36.38	15,609	16,500	+5.71

Table 8. Performance criteria and entropy generation at φ = 5%, Re = 20,000, d_p = 30 nm, counter flow (Eqs. (18)–(22))

Fluid	PEC_h	EER	$N_{s,a}$	S^*	Be
Al_2O_3	1.0941	0.9326	1.0117	0.9768	0.99987
CuO	1.1316	1.1036	0.9743	0.9670	0.99989
TiO_2	1.0824	0.9477	1.0042	0.9775	0.99988

Note: Performance-evaluation criteria (PEC), energy-efficiency ratio (EER); $S^* = (\dot{S}_{gen}/Q)/(\dot{S}_{gen,0}/Q_0)$, the entropy generation per unit duty relative to water.

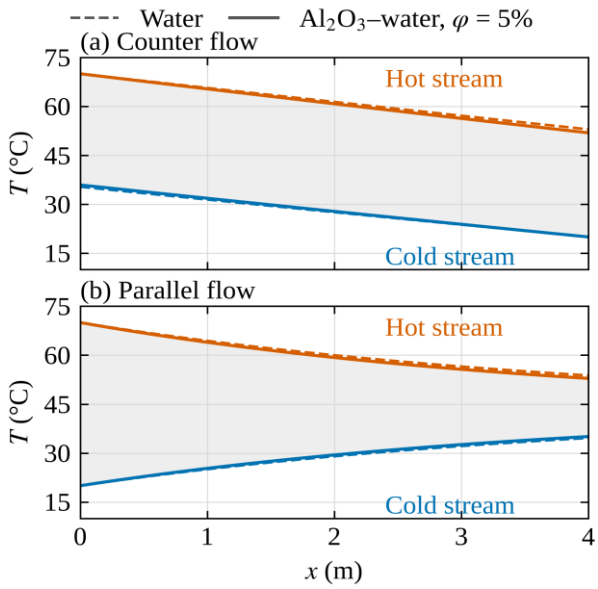


Figure 7. Axial temperature distributions of water and Al_2O_3–water (φ = 5%) at Re = 20,000, obtained from Eq. (17): (a) counter flow; (b) parallel flow

With respect to the second law, $N_{s,a}$ (Eq. (22)) fell below unity only for CuO, to 0.9743, a 2.6% reduction in total irreversibility relative to pure water (Table 8). Al_2O_3 and TiO_2 increased the total slightly, by 1.2% and 0.4%, respectively, because the additional duty they transferred was accompanied by additional thermal irreversibility. Per unit duty, however, all three nanofluids generated less entropy than water. For water at Re = 20,000, the thermal term was 5.39 W K^{-1} (−48.01 W K^{-1} on the hot side and +53.40 W K^{-1} on the cold side), whereas the frictional term was only 6.3 × 10^{-4} W K^{-1}. The Bejan number therefore exceeded 0.9998 for $Re \le 20{,}000$ and remained above 0.9989 at Re = 50,000. The irreversibility was thus dominated by heat transfer rather than by friction over the whole range studied.

Finally, a compact correlation for the ratio of the convective coefficients was fitted separately for each material:

$$\frac{h_{nf}}{h_{bf}} = 1 + K\varphi^{a}\left(\frac{d_p}{D_{i,in}}\right)^{b}\left(\frac{T_{avg}}{T_{ref}}\right)^{c} \tag{23}$$

In Eq. (23), φ is the volume fraction expressed as a fraction, d_p and $D_{i,in}$ are both in m ($D_{i,in}$ = 0.022 m), T_{avg} is the bulk-mean evaluation temperature in K, and $T_{ref} = T_{c,in}$ = 293.15 K. The fitting data comprised 525 points per material (1,575 in total): five non-zero volume fractions (1–5%) and three particle diameters, each combined with 35 pairs of Reynolds number (5,000–50,000) and hot-side inlet temperature (50–90 °C). The flow arrangement was not varied because h_i is independent of the arrangement when the properties are evaluated at a fixed temperature. The Reynolds number was varied but omitted from Eq. (23) because its effect on the ratio is weak: at φ = 5%, h_{nf}/h_{bf} for Al_2O_3 changed only from 1.149 to 1.124 between Re = 5,000 and 50,000. This residual dependence is the main source of the scatter in Figure 8.

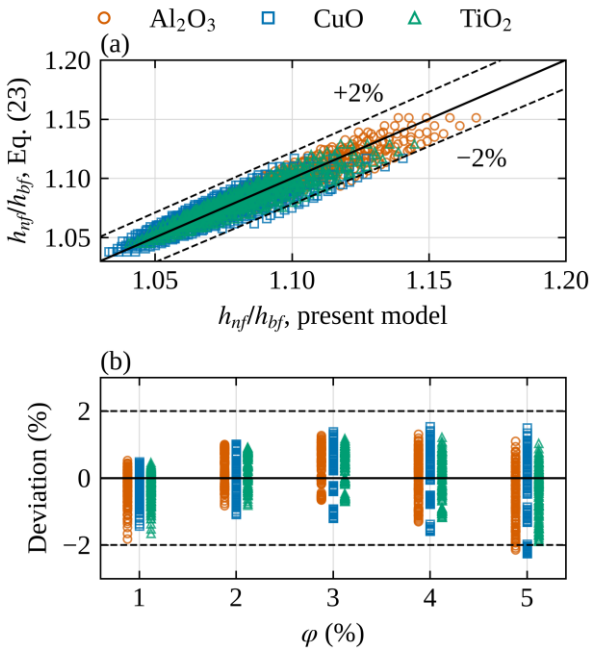


Figure 8. Proposed correlation, Eq. (23): (a) parity plot; (b) residual distribution

The coefficients are listed in Table 9. The exponent on the volume fraction is close to one third, so the enhancement grows sub-linearly with concentration. The negative exponent on the particle diameter reflects the stronger effect of finer particles, and the large positive exponent on temperature reflects the strength of the Brownian contribution. On the fitting data, the mean absolute error was below 0.7% and the maximum error below 2.3% (Figure 8). The correlation was also assessed on an independent hold-out set of 192 points per material that were not used in the fit (φ = 1.5, 2.5, 3.5 and 4.5%; d_p = 35, 50 and 55 nm; Re = 7,500, 15,000, 25,000 and 42,500; $T_{h,in}$ = 55, 65, 75 and 85 °C). On this set, the mean

absolute errors were 0.45%, 0.53% and 0.42% and the maximum errors 1.27%, 1.35% and 1.13% for Al_2O_3, CuO and TiO_2, respectively. Both data sets were generated by the same model. The correlation therefore reproduces the model and inherits its assumptions and validity limits.

Table 9. Coefficients and accuracy of the proposed correlation (Eq. (23))

Fluid	10^3K	a	b	c	MAE (%)	Max (%)	MAE_{ho} (%)
Al_2O_3	6.515	0.3801	−0.2791	4.5637	0.566	2.138	0.447
CuO	1.012	0.3026	−0.3683	6.0720	0.676	2.252	0.529
TiO_2	2.884	0.3195	−0.3100	5.0835	0.524	1.882	0.415

Note: Mean absolute error (MAE) and maximum (Max) refer to the fitting data and MAE_{ho} to the hold-out set. Validity: $5{,}000 \le Re \le 50{,}000$; $1\% \le \varphi \le 5\%$; $30\ \text{nm} \le d_p \le 60\ \text{nm}$; $50\ ^\circ\text{C} \le T_{h,in} \le 90\ ^\circ\text{C}$ (308.15 K ≤ T_{avg} ≤ 328.15 K).

6.6 Overall assessment and material selection

No single material was optimal on every metric. Al_2O_3 gave the largest convective-coefficient enhancement and duty, but also the largest pressure-drop increase. TiO_2 was intermediate on all metrics. CuO gave the smallest enhancement, yet it combined the smallest hydraulic penalty with the highest effectiveness, the highest PEC_h and the only reduction in total entropy generation. When the thermal gain and the hydraulic penalty are weighed together, CuO is therefore the preferred working fluid for the present geometry, the fixed-*Re* basis and the operating conditions of Table 2.

6.7 Limitations

Four limitations should be noted. First, the single-phase treatment does not resolve particle migration or thermophoretic drift and is known to under-predict measured enhancements [24, 28]. Second, the properties were constant along the exchanger, with the base-fluid properties held at 40 °C (Section 2.1). Third, the Al_2O_3 Brownian coefficient was used for TiO_2 (Section 3.1). Fourth, the ranking was obtained at a fixed Reynolds number for a single geometry; other comparison bases may change it (Section 6.3).

7. CONCLUSIONS

CuO, Al_2O_3 and TiO_2 water-based nanofluids were compared in a straight double-pipe heat exchanger with a verified MATLAB model based on the Koo–Kleinstreuer conductivity model. The main conclusions are as follows:

(1) The choice of conductivity model is decisive: the Koo–Kleinstreuer model predicts more than twice the enhancement of the classical Maxwell model, so enhancement values should always be reported together with the model used.

(2) Al_2O_3 gave the largest convective-coefficient enhancement and the highest duty, whereas CuO gave the smallest enhancement but the highest effectiveness, because of its low specific heat.

(3) At a fixed Reynolds number, the pressure-drop penalty separated the nanofluids far more sharply than the thermal gain and was smallest for CuO, the densest material. This hydraulic advantage is a consequence of the comparison basis and of the Brinkman viscosity relation.

(4) CuO ranked first on the coefficient-based performance criterion and was the only nanofluid that reduced the total entropy generation relative to water. The irreversibility was dominated by heat transfer throughout.

(5) Smaller particles, higher operating temperatures and the counter-flow arrangement each increased the thermal benefit, the first two through the Brownian term, which classical mixture models cannot reproduce.

(6) For the present geometry and operating conditions, CuO offers the most favourable combined thermal–hydraulic performance. Al_2O_3 is preferable only where maximum duty is the sole objective and the pumping penalty is acceptable.

The proposed correlation, Eq. (23), can be used for rapid design estimates within its validity range. Future work should include a two-phase treatment of particle migration, temperature-dependent properties along the exchanger, a dedicated Brownian coefficient for TiO_2–water and comparisons on other bases, such as equal pumping power.

ACKNOWLEDGMENT

The authors thank the College of Engineering, Wasit University, and the Faculty of Engineering, University of Misan, for their academic support. This research did not receive any specific grant from funding agencies in the public, commercial or not-for-profit sectors.

REFERENCES

[1] Purbia, D., Khandelwal, A., Kumar, A., Sharma, A.K. (2019). Graphene-water nanofluid in heat exchanger: Mathematical modelling, simulation and economic evaluation. International Communications in Heat and Mass Transfer, 108: 104327. https://doi.org/10.1016/j.icheatmasstransfer.2019.104327

[2] Rashid, F.L., Al-Obaidi, M.A., Al Maimuri, N.M.L., et al. (2025). Enhancing efficiency in double-pipe heat exchangers: A detailed review of nanofluids and their impact on thermal performance. Heat Transfer, 55(1): 212-240. https://doi.org/10.1002/htj.70070

[3] Cardoso, B.D., Souza, A., Nobrega, G., et al. (2025). Progress in nanofluid technology: From conventional to green nanofluids for biomedical, heat transfer, and machining applications. Nanomaterials, 15(16): 1242. https://doi.org/10.3390/nano15161242

[4] Aleuaysh, A.Z.N. (2026). Thermal performance enhancement of heat exchangers using nano-fluid in energy conversion systems. Dijlah Journal of Engineering Sciences, 3(2): 71-95. https://doi.org/10.65204/djes.v3i2.517

[5] Nayebpashaee, N. (2026). Experimental investigation of thermophysical properties of Al_2O_3 TiO_2 CuO Fe_3O_4 water ethylene glycol quadri hybrid nanofluid. Discover Nano, 21: 142. https://doi.org/10.1186/s11671-026-04602-w

[6] Ghazanfari, V., Taheri, A., Amini, Y., Mansourzade, F. (2024). Enhancing heat transfer in a heat exchanger: CFD study of twisted tube and nanofluid (Al_2O_3, Cu, CuO and TiO_2) effects. Case Studies in Thermal Engineering, 53: 103864. https://doi.org/10.1016/j.csite.2023.103864

[7] Jasim, Q.K., Saleh, N.M., Hussein, A.M. (2020). Improving thermal performance using Al_2O_3–water

nanofluid in a double-pipe heat exchanger filled with a porous medium. Thermal Science, 24(6B): 4267-4275. https://thermalscience.rs/pdfs/papers-2020/TSCI190602056J.pdf.

[8] Jassim, E.I., Ahmed, F. (2020). Experimental assessment of Al_2O_3 and Cu nanofluids on the performance and heat leak of a double-pipe heat exchanger. Heat and Mass Transfer, 56: 1845-1858. https://doi.org/10.1007/s00231-020-02826-9

[9] Kannadhasan, V., Senthil Kumar, A., Vairamuthu, J., Nagarajan, R. (2022). Experimental research and CFD analysis on a double-pipe heat exchanger with CuO nanoparticles suspended in cold water. Journal of Thermal Analysis and Calorimetry, 147: 3831-3838. https://doi.org/10.1007/s10973-021-10804-4

[10] Jalili, B., Aghaee, N., Jalili, P., Ganji, D.D. (2022). Novel usage of the curved rectangular fin on the heat transfer of a double-pipe heat exchanger with a nanofluid. Case Studies in Thermal Engineering, 35: 102086. https://doi.org/10.1016/j.csite.2022.102086

[11] Nam, H.T., Lee, S., Kong, M., Lee, S. (2023). Numerical study of flow and heat transfer characteristics for Al_2O_3 nanofluid in a double-pipe helical coil heat exchanger. Micromachines, 14(12): 2219. https://doi.org/10.3390/mi14122219

[12] Bantan, R.A.R., Abu-Hamdeh, N.H., AlQemlas, T., Elamin, A.E.A.M.A. (2023). Heat transfer improvement of hybrid nanofluid with the use of twisted tapes within a heat exchanger. Alexandria Engineering Journal, 70: 673-684. https://doi.org/10.1016/j.aej.2023.03.016

[13] Azizi, Y., Bahramkhoo, M., Kazemi, A. (2023). Influence of non-uniform magnetic field on the thermal efficiency hydrodynamic characteristics of nanofluid in double pipe heat exchanger. Scientific Reports, 13: 407. https://doi.org/10.1038/s41598-022-26285-w

[14] Salim, A., Jihan, J.I., Das, B.K., Ahmed, M.R. (2024). Thermal performance investigation of N-shape double-pipe heat exchanger using Al_2O_3, TiO_2 and Fe_3O_4-based nanofluids. Energy Science & Engineering, 12(3): 1072-1090. https://doi.org/10.1002/ese3.1698

[15] Ajeeb, W., da Silva, R.R.T., Murshed, S.M.S. (2023). Experimental investigation of the heat-transfer performance of Al_2O_3 nanofluids in a compact plate heat exchanger. Applied Thermal Engineering, 218: 119321. https://doi.org/10.1016/j.applthermaleng.2022.119321

[16] Alhulaifi, A.S. (2024). Computational fluid dynamics heat transfer analysis of a double-pipe heat exchanger and flow characteristics using TiO_2 with water. Designs, 8(3): 39. https://doi.org/10.3390/designs8030039

[17] Kadhim, S.A., Askar, A.H., Saleh, A.A.M. (2024). An enhancement of double-pipe heat exchanger performance at a constant wall temperature using a nanofluid of iron oxide and refrigerant vapour. Journal of Thermal Engineering, 10(1): 78-87. https://doi.org/10.18186/thermal.1429191

[18] Kadhim, S.A., Hammoodi, K.A., Askar, A.H., Rashid, F.L., Abdul Wahhab, H.A. (2024). Feasibility review of using copper-oxide nanofluid to improve heat transfer in a double-tube heat exchanger. Results in Engineering, 24: 103227. https://doi.org/10.1016/j.rineng.2024.103227

[19] Gabir, M.M., Albayati, I.M., Hatami, M., Alkhafaji, D. (2024). An experimental investigation of the convective heat transfer augmentation in U-bend double pipe heat exchanger using water-MgO-Cmc fluid. Scientific Reports, 14: 12442. https://doi.org/10.1038/s41598-024-63043-6

[20] Abdelmagied, M. (2025). Numerical analysis of heat-transfer enhancement of Al_2O_3 and CuO-water nanofluids in annular curved tubes. International Journal of Air-Conditioning and Refrigeration, 33: 1. https://doi.org/10.1007/s44189-024-00066-8

[21] Mousazadeh, M., Sarmasti Emami, M.R., Afsari, K. (2025). Experimental assessment of $MnCoFeO_4$@H_2O nanofluid stability and its impact on heat-transfer enhancement in a double pipe heat exchanger. Results in Engineering, 27: 106022. https://doi.org/10.1016/j.rineng.2025.106022

[22] Canbolat, G. (2026). Numerical and theoretical investigation of thermal performance in double pipe heat exchanger using nanofluids with integrated CFD and ANN methods. Arabian Journal for Science and Engineering, 51: 21743-21760. https://doi.org/10.1007/s13369-026-11185-2

[23] Kern, D.Q. (1950). Process Heat Transfer. McGraw-Hill, New York.

[24] Aghayari, R., Maddah, H., Zarei, M., Dehghani, M., Ghanbari Kaskari Mahalle, S. (2014). Heat transfer of nanofluid in a double pipe heat exchanger. International Scholarly Research Notices, 2014(1): 736424. https://doi.org/10.1155/2014/736424

[25] Koo, J., Kleinstreuer, C. (2004). A new thermal conductivity model for nanofluids. Journal of Nanoparticle Research, 6: 577-588. https://doi.org/10.1007/s11051-004-3170-5

[26] Vajjha, R.S., Das, D.K. (2009). Experimental determination of thermal conductivity of three nanofluids and development of new correlations. International Journal of Heat and Mass Transfer, 52(21-22): 4675-4682. https://doi.org/10.1016/j.ijheatmasstransfer.2009.06.027

[27] Zheng, M.R., Han, D., Asif, F., Si, Z.T. (2020). Effect of Al_2O_3/water nanofluid on heat transfer of turbulent flow in the inner pipe of a double-pipe heat exchanger. Heat and Mass Transfer, 56: 1127-1140. https://doi.org/10.1007/s00231-019-02774-z

[28] Saha, G., Paul, M.C. (2014). Numerical analysis of the heat transfer behaviour of water based Al_2O_3 and TiO_2 nanofluids in a circular pipe under the turbulent flow condition. International Communications in Heat and Mass Transfer, 56: 96-108. https://doi.org/10.1016/j.icheatmasstransfer.2014.06.008

[29] Pak, B.C., Cho, Y.I. (1998). Hydrodynamic and heat transfer study of dispersed fluids with submicron metallic oxide particles. Experimental Heat Transfer, 11(2): 151-170. https://doi.org/10.1080/08916159808946559

[30] Xuan, Y.M., Roetzel, W. (2000). Conceptions for heat transfer correlation of nanofluids. International Journal of Heat and Mass Transfer, 43(19): 3701-3707. https://doi.org/10.1016/S0017-9310(99)00369-5

[31] Brinkman, H.C. (1952). The viscosity of concentrated suspensions and solutions. The Journal of Chemical Physics, 20(4): 571. https://doi.org/10.1063/1.1700493

[32] Maxwell, J.C. (1881). A Treatise on Electricity and Magnetism, 2nd ed. Clarendon Press, Oxford.

[33] Hamilton, R.L., Crosser, O.K. (1962). Thermal

conductivity of heterogeneous two-component systems. Industrial & Engineering Chemistry Fundamentals, 1(3): 187-191. https://doi.org/10.1021/i160003a005
[34] Gnielinski, V. (1976). New equations for heat and mass transfer in turbulent pipe and channel flow. International Chemical Engineering, 16(2): 359-368.
[35] Dittus, F.W., Boelter, L.M.K. (1985). Heat transfer in automobile radiators of the tubular type. Reprinted in International Communications in Heat and Mass Transfer, 12(1): 3-22. https://doi.org/10.1016/0735-1933(85)90003-X
[36] Petukhov, B.S. (1970). Heat transfer and friction in turbulent pipe flow with variable physical properties. Advances in Heat Transfer, 6: 503-564. https://doi.org/10.1016/S0065-2717(08)70153-9
[37] Maïga, S.E.B., Nguyen, C.T., Galanis, N., Roy, G., Maré, T., Coqueux, M. (2006). Heat-transfer enhancement in turbulent tube flow using Al_2O_3 nanoparticle suspension. International Journal of Numerical Methods for Heat & Fluid Flow, 16(3): 275-292. https://doi.org/10.1108/09615530610649717
[38] Xuan, Y.M., Li, Q. (2003). Investigation on convective heat transfer and flow features of nanofluids. Journal of Heat Transfer, 125(1): 151-155. https://doi.org/10.1115/1.1532008
[39] Bejan, A. (1995). Entropy Generation Minimization: The Method of Thermodynamic Optimization of Finite-Size Systems and Finite-Time Processes. CRC Press, Boca Raton. https://doi.org/10.1201/9781482239171

NOMENCLATURE

A	heat-transfer surface area, m²
a, b, c	exponents of Eq. (23), dimensionless
Be	Bejan number, Eq. (22), dimensionless
C	heat-capacity rate, $\dot{m}c_p$, W K^{-1}
C_r	heat-capacity ratio, dimensionless
c_p	specific heat capacity, J kg^{-1} K^{-1}
D	diameter, m
D_h	hydraulic diameter of the annulus, m
d_p	nanoparticle diameter, m (reported in nm)
EER	energy-efficiency ratio, Eq. (19), dimensionless
f	Darcy friction factor, dimensionless
g	Brownian temperature function, Eq. (8), dimensionless
h	convective heat-transfer coefficient, W m^{-2} K^{-1}
K	coefficient of Eq. (23), dimensionless
k	thermal conductivity, W m^{-1} K^{-1}
k_B	Boltzmann constant, 1.381×10^{-23} J K^{-1}
L	exchanger length, m
$\dot{m}$	mass flow rate, kg s^{-1}
$N_{s,a}$	augmentation entropy-generation number, Eq. (22), dimensionless
NTU	number of transfer units, dimensionless
Nu	Nusselt number, dimensionless
P	pumping power, W
PEC	performance-evaluation criterion, dimensionless
PEC_h	coefficient-based performance-evaluation criterion, Eq. (18), dimensionless
Pr	Prandtl number, dimensionless
Q	heat-transfer rate (duty), W
Re	Reynolds number, dimensionless
$\dot{S}_{gen}$	entropy-generation rate, W K^{-1}
S^*	entropy generation per unit duty relative to water (Table 8), dimensionless
T	temperature, K or °C
T_{avg}	bulk-mean (property-evaluation) temperature, K
T_0	reference temperature of Eq. (8), 273 K
T_{ref}	reference temperature of Eq. (23), 293.15 K
$\bar{T}$	arithmetic-mean stream temperature, K
U	overall heat-transfer coefficient (based on A_i), W m^{-2} K^{-1}
v	mean velocity, m s^{-1}
x	axial coordinate, m

Greek symbols

β	Brownian-motion coefficient, Eq. (7), dimensionless
ΔP	pressure drop, Pa
Δh	relative enhancement of the convective heat-transfer coefficient, %
ε	effectiveness, dimensionless
μ	dynamic viscosity, Pa s
ρ	density, kg m^{-3}
φ	nanoparticle volume fraction, dimensionless (reported in %)

Subscripts

0	base fluid at the same operating conditions
bf	base fluid (water)
c	cold side
cf, pf	counter flow, parallel flow
fr	frictional
h	hot side
i	inner tube
in, out	inlet, outlet
max, min	maximum, minimum
nf	nanofluid
o	outer tube (annulus)
p	nanoparticle
static, Brownian	static (Maxwell) and Brownian contributions
th	thermal
wall	tube wall